Crystal–chemical and biological controls of elemental incorporation into magnetite nanocrystals

Matthieu Amor, J. Frederick W. Mosselmans, Ernesto Scoppola, Chenghao Li, Damien Faivre, Daniel Chevrier

Crystal-chemical and biological controls of trace and minor element incorporation into magnetite nanocrystals

Matthieu Amor[a ⊥*], *J. Frederick W. Mosselmans*[b], *Ernesto Scoppola*[c], *Chenghao Li*[c], *Damien Faivre*[a], *Daniel M. Chevrier*[a *]

[a] *Aix-Marseille Université, CEA, CNRS, BIAM, 13108 Saint-Paul-lez-Durance, France*

[b] *Diamond Light Source, Diamond House, Harwell Campus, Chilton, Didcot, OX11 0DE, United Kingdom*

[c] *Biomaterials, Hierarchical Structure of Biological and Bio-inspired Materials, Max Planck Institute of Colloids and Interfaces, Potsdam 14476, Germany*

⊥ Present address: Univ. Lyon, ENSL, UCBL, UJM, CNRS, LGL-TPE, F-69007 Lyon, France

* To whom correspondence should be addressed:
matthieu.amor@ens-lyon.fr (MA); daniel.chevrier@cea.fr (DMC)

Abstract

Magnetite nanoparticles possess numerous fundamental, biomedical and industrial applications, many of which depend on tuning the magnetic properties. This is often achieved by the incorporation of trace and minor elements into the magnetite lattice. Such incorporation was shown to depend strongly on the magnetite formation pathway (*i.e.*, abiotic *vs* biological), but the mechanisms controlling element partitioning between magnetite and its surrounding precipitation solution remain to be elucidated. Here, we used a combination of theoretical modelling (lattice and crystal field theories) and experimental evidence (high-resolution inductively coupled plasma mass spectrometry and X-ray absorption spectroscopy) to demonstrate that element incorporation into abiotic magnetite nanoparticles is controlled principally by cation size and valence. Elements from the first series of transition metals (Cr to Zn) constituted exceptions to this finding as their incorporation appeared to be also controlled by the energy levels of their unfilled 3d orbitals, in line with crystal field mechanisms. We finally show that element incorporation into biological magnetite nanoparticles produced by magnetotactic bacteria (MTB) cannot be explained by crystal-chemical parameters alone, which points to the biological control exerted by the bacteria over the element transfer between MTB growth medium and the intracellular environment. This screening effect generates biological magnetite with a purer chemical composition than the abiotic materials formed in a solution of similar composition. Our work establishes a theoretical framework for understanding the crystal-chemical and biological controls of trace and minor cation incorporation into magnetite, thereby providing predictive methods to tailor the composition of magnetite nanoparticles for improved control over magnetic properties.

Keywords: Trace Element Partitioning, Magnetotactic Bacteria, Magnetite Nanoparticles, Biomineralization, Lattice and Crystal Field Theories

Main Text

Magnetite [$Fe(II)Fe(III)_2O_4$] is a naturally-occurring ubiquitous Fe oxide that can be precipitated through abiotic chemical reactions.[1] Microorganisms can also promote magnetite formation. Among them, only magnetotactic bacteria (MTB) are known to synthesize nanoparticles of magnetite in a genetically controlled manner by incorporating Fe into organelles called magnetosomes for magnetite formation.[2] MTB are proposed to represent some of the most ancient microorganisms on Earth,[3] and are markers of oxic/anoxic transitions in the environment.[4] Nanoparticles of magnetite are of fundamental scientific interest in industrial and biomedical applications,[5,6,7] with many of these interests relying on careful tuning and optimization of magnetic properties. A particular way of doing so directly relies on modifying the chemical composition of magnetite, into which cations can substitute for Fe, incorporating into the magnetite lattice structure and thereby modifying its magnetic properties such as coercivity, saturation magnetization or heat release capacity.[8,9] Cation incorporation has been shown to depend strongly on the nature of the magnetite formation pathways (*i.e.*, abiotic or biologic),[10] but the mechanisms controlling such incorporation remain unknown.

The content of trace and minor elements in magnetite is also of critical interest for the detection of extra-terrestrial and ancient terrestrial life[4] as exemplified by the controversial origin of magnetite in the Martian meteorite ALH84001.[11] This meteorite contains nanocrystals of magnetite encapsulated in (Ca, Mg, Fe)-carbonates showing a pure chemical composition (*i.e.*, they contain no detectable dopant elements).[12] They were proposed to be produced from the thermal decomposition of the carbonate matrix,[13] although laboratory experimentation showed that incorporation of Mg and Ca into the generated magnetite should occur during such processes.[14] An alternative biological origin of this Martian magnetite was thus suggested, since only MTB were shown to generate magnetite with pure chemical composition.[10] Such characteristic property of biological magnetite was proposed as a reliable tool for the identification of fossils of MTB in ancient terrestrial and extra-terrestrial environments.[4] Therefore, understanding the mechanisms leading to trace and minor element incorporation into magnetite, as well as the capacity of MTB to screen for element incorporation, has important implications in exobiology and (paleo)environmental sciences.[4]

The goal of the present work is to establish the crystal-chemical parameters controlling the incorporation of trace and minor elements into magnetite nanocrystals. Scheme 1 illustrates the partitioning of tested elements into magnetite nanocrystals of synthetic and biological origin. Using the concentrations of chemical elements in magnetite and residual solution ($[X]_{magnetite}$ and $[X_{solution}]$, respectively) measured from high-resolution inductively coupled plasma mass

spectrometry (HR-ICP-MS)[10] in abiotic magnetite, we show that the cation incorporation is controlled by the ionic radius and the valence. Identifying this comprehensive framework of the crystal-chemical processes controlling element incorporation into magnetite enables us to investigate the biological control exerted by the magnetotactic strain *Magnetospirillum magneticum* AMB-1 on element partitioning between magnetite and the external solution.[10] We find that the behavior of elements during biological formation of magnetite cannot be explained by crystal-chemical parameters alone: their incorporation into MTB magnetite is more limited than expected given their ionic radius and valence. These results point towards an active screening of elements by the bacteria to limit the transfer of trace and minor elements from the external solution to internally formed magnetite nanoparticles.

We report a few exceptions to this general picture: elements from the first series of transition metals (Cr, Mn, Co, Ni, Cu, Zn) are more stabilized into the magnetite lattice during abiotic precipitation than predicted from their size and valence, but they do not show any specific behavior in AMB-1. To establish the consistency of these findings as well as their crystal-chemical and biological relevance, we prepared a second round of abiotic and biological magnetite samples produced in the presence of Co, Mn and Zn following distinct protocols. Abiotic magnetite was synthesized at constant pH using a titration device. The incorporation behavior of Co, Mn and Zn into MTB-produced magnetite was then confirmed by cultivating a distinct magnetotactic strain (*Magnetospirillum gryphiswaldense* MSR-1) to test the potential biological variability of iron-series metal incorporation in MTB induced by distinct bacterial strains. The choice of MSR-1 was motivated by the extensive literature characterizing the coordination of transition metals in MSR-1 magnetite using X-ray spectroscopy (XAS). HR-ICP-MS analyses of abiotic magnetite produced in the titration device yielded results similar to those produced in batch, validating the enhanced stabilization of 3d metals in magnetite. In addition, Co, Mn and Zn incorporation into MSR-1 magnetite was also similar to what was previously observed in AMB-1, demonstrating that these elements have no specific behavior during magnetite precipitation in either strain of MTB. X-ray absorption spectroscopy (XAS) analyses specifically on Co, Mn and Zn were performed to confirm the incorporation into the magnetite nanocrystals and to identify the possible local structure of these metals, helping to reveal the origin of their enhanced stabilization in abiotic magnetite. They demonstrate that the preferential incorporation of first series transition metals can be explained by the energy levels of unfilled 3d electron orbitals according to the crystal field theory, and further demonstrate the active screening of trace elements induced by MTB.

Results and Discussion

Chemical composition of abiotic and biological magnetite

Magnetite possesses an inverse spinel structure, with trivalent cations [Fe(III)] contained in both octahedral (6-coordination) and tetrahedral sites (4-coordination) while divalent cations [Fe(II)] occupy octahedral sites only.[1] During abiotic or biological formation, distinct trace and minor cations can substitute Fe(II) or Fe(III) by incorporating into the lattice structure. A previous study quantified the trace element content of abiotic and biological (AMB-1 strain) magnetite nanoparticles.[10] Magnetite nanoparticles were thoroughly purified in order to eliminate adsorbed elements (see ref.[10] for high-resolution TEM). X-ray diffraction and high-resolution electron microscopy analyses of the samples revealed pure magnetite crystals, with no additional precipitated phases potentially induced by element doping.[10] The concentrations of trace and minor elements (X) in magnetite and in the residual solution after nanoparticle formation were measured using HR-ICP-MS. For each element, a partition coefficient (D^X) between magnetite and solution was calculated from the equation:

$$D^X = \frac{[X_{magnetite}]}{[X_{solution}]} \quad (1)$$

where $[X_{magnetite}]$ and $[X_{solution}]$ are the massic concentrations of an element X in magnetite and in the residual solution after precipitation, respectively, expressed in ppb. Thus, the partition coefficient quantifies the capacity of an element to incorporate into magnetite and does not depend on the initial concentration of trace elements in the precipitation solution, at least in first approximation. We show below that element partitioning can be explained by crystal-chemical parameters according to established models, demonstrating that the element concentration used (100 ppb for each element) did not induce competition between elements for incorporation into magnetite. The same set of partition coefficients was calculated in the case of biological formation by AMB-1 with identical dopant concentrations in the initial study.[10] Elemental concentrations in the residual growth media as well as magnetite samples thoroughly purified were quantified using HR-ICP-MS. Measured elemental concentrations and partition coefficients are given in Tables S1 and S2.

Lattice strain control of element incorporation into magnetite

The partitioning of a trace element between a given lattice site (M) and melts under high temperature and pressure conditions is controlled by the ion radius and valence.[15] For a given valence (n+, with n = 1, 2, 3 or 4), incorporation of a trace element is maximized when the ionic

radius (r^X) matches the size of the site M ($r_{n+}^{0(M)}$). A shift from this ideal size generates an elastic deformation that is accommodated by the neighboring crystal lattice, translating into a penalty in energy for the ion incorporation and, consequently, into a decrease of D^X. A size shift of the same magnitude but with opposite sign corresponds to the same energy penalty. The distribution of D^X values for an isovalent series of elements thus follows a parabolic trend with a maximum value ($D_{n+}^{0(M)}$) corresponding to a fictive element perfectly matching the size of the lattice site (*i.e.*, strain-compensated D^X)[15] (see Eqs. 2 and 3 in Materials and Methods). Similarly, heterovalent cation substitution entails accommodation of excess electric charge by the crystal lattice that will also translate into a penalty in energy for element incorporation.[15] Thus, $D_{n+}^{0(M)}$ corresponding to each valence also follow a parabolic trend with a maximum coefficient $D^{00(M)}$ corresponding to an ion causing no electrostatic charging (*i.e.*, homovalent substitution).

We tested such a model in the case of magnetite to determine the role of ion radius and valence in the distribution of D^X but under different conditions at ambient temperature and atmospheric pressure. For all valences, the experimentally determined D^X plotted against their cation radius were close to the predicted values calculated from Eq. 2 (Fig. 1). This shows that the incorporation of most trace and minor elements into abiotic magnetite can be predicted by a lattice strain model. The strain-compensated $D_{n+}^{0(M)}$extracted from Fig. 1 and represented against ionic charge also followed the expected parabolic trend (Fig. 2) (Eq. 3). The maximum $D_{n+}^{0(M)}$ corresponding to $D^{00(M)}$ was observed for a cation charge of +2.7, almost identical to the bulk Fe valence in magnetite (+2.67). Overall, the distribution of D^X values determined experimentally in abiotic precipitation followed a lattice strain model, demonstrating that cation radius and valence control the incorporation of trace and minor elements in abiotic magnetite. However, a few exceptions were observed: Cr(II), Cr(III), Mn(II), Co(II), Ni(II), Cu(II) and Zn(II) (grey circles in Fig. 1), which all belong to the first series of transition metals (3d metals) also containing Fe, showed higher D^X than expected from their radii and valence. Such preferential incorporation cannot be explained by potential co-precipitation of distinct (oxyhydr)oxides phases as shown by X-ray diffraction and electron microscopy performed on the samples used for the determination of D^X.[10]

Next, we consider the partition coefficients of trace and minor elements between the biological magnetite and the growth medium, which shows a distinct picture from abiotic results (Fig. 1). D^X values were consistently lower than those predicted from a lattice strain model (Eq. 2). Such depletion corresponds to a factor of ~5 x 10^1 [Cs(I)] up to ~9 x 10^7 [La(III)]. The range of variation for D^X was also narrower in the case of biological magnetite, with most

values ranging between 10^{-1} and 10^{2}, compared to the D^X variation in abiotic magnetite of 7 orders of magnitude (Rb to Bi). Finally, the distribution of partition coefficients could not be modeled by the lattice strain theory using Eq. 2, showing that crystal-chemical parameters cannot explain the partitioning of trace and minor elements between AMB-1 magnetite and the external growth medium.

Biological control over element transfer to magnetosomes in magnetotactic bacteria

Our work aims at understanding the mechanisms controlling the incorporation of cations distinct from Fe into magnetite. It demonstrates that partitioning of trace and minor elements between abiotic magnetite and surrounding solution is controlled by cation radius and valence (with the exception of the first series of transition metals, see below for details). The biological case showed a distinct picture as the distribution of D^X could not be modeled from lattice strain. MTB selectively incorporate Fe into the intracellular medium, and sequester it in magnetosome for magnetite formation thus excluding distinct trace and minor elements that cannot substitute with Fe for their incorporation into magnetite. The low partition coefficients and low variation of D^X in the biological conditions are in line with the proposed hypothesis of Fe biopurification during magnetite formation, establishing the chemical purity of magnetite as a signature of MTB activity.

MTB precipitate magnetite in lipid vesicles (*i.e.*, the intramagnetosomal environment), which are physically separated from the extracellular medium. They create local specific intracellular environments in magnetosomes with defined chemical conditions (pH, redox potential etc.) that allow magnetite formation.[16] The variability induced by MTB on trace and minor element partitioning could arise from the homeostasis of chemical conditions in the intracellular environment, which are distinct from the external solution and maintained by the metabolic activity of the bacteria.[16–18] These chemical conditions control the cation valence and speciation (and thus its size) in solution, which may in turn shift element partitioning (Eqs 2 and 3, Figs. 1 and 2). However, the variability of cation size and valence evidenced by XAS measurements (see below) is too low to account for the decrease of D^X in the biological conditions (up to 7 orders of magnitude, see Fig. 1).

Although not demonstrated, the lower levels of doped cations in biological magnetite were discussed as being caused by active and selective Fe incorporation into magnetosomes that excludes distinct elements.[10] A notable difference between both conditions of magnetite precipitation is the decrease of partition coefficients in bacterial cultures as all elements showed lower D^X values than those predicted from the lattice strain theory (Fig. 1). The range of

partition coefficients was also narrower in AMB-1 cultures compared to abiotic magnetite (Fig. 1). Consequently, the enrichment of trace elements in AMB-1 magnetite quantified by the ratio of measured D^X normalized to D^X values predicted from the lattice strain theory decreases linearly with the increase of cation radius, down to the ideal size ($r_{n+}^{0(M)}$) that is associated with the maximum D^X (Fig. 3). Enrichment of doping elements in MTB magnetite then increases again for cation radii higher than $r_{n+}^{0(M)}$ (Figs. 3A and 3D). Accordingly, the depletion of trace and minor elements from MTB magnetite is higher for elements showing high affinity for magnetite, and minimal for cations with the lowest abiotic D^X (Fig. 3). This illustrates a screening effect induced by the bacterial membranes that limits the transfer of cations distinct from Fe from the external solution to the location of magnetite formation regardless of the cation size and valence. Silver was one exception to this picture, as it was more enriched in AMB-1 magnetite than the rest of the monovalent elements (Fig. 3A). This could reflect the antimicrobial properties of Ag(I)[19] and its sequestration into magnetite for detoxification as previously proposed for toxic cations.[20] Alternatively, such preferential inclusion of Ag in AMB-1 could arise from passive diffusion between the external solution and the intracellular medium.

Investigating the crystal-chemical properties of trace and minor elements belonging to the first series of transition metals

We show in Fig. 1 that elements from the first series of transition metals (Cr, Mn, Co, Ni, Cu and Zn) behave in a distinct manner from other metal groups: their partitioning could not be explained from the lattice strain theory with D^X values higher than those predicted. Such enhanced incorporation was not evidenced in the case of biological magnetite produced by AMB-1. To ensure that these observations are real and were not generated by specific precipitation conditions or bacterial strain, we performed additional magnetite syntheses with a mixture of Co, Mn and Zn using distinct protocols and bacterial strain. The choice of metals is made by their frequent use as dopants to tune magnetic properties of magnetite.[8,9,21] First, abiotic magnetite nanoparticles were synthesized using a titration device (see Materials and Methods) following a well-established protocol to produce highly pure magnetite.[22–24] Using this device, the pH of the precipitation solution is kept constant over magnetite precipitation by adding NaOH solution, and the Fe, Co, Mn and Zn mixture is progressively added to the precipitation solution. In addition, the magnetotactic strain *Magnetospirillum gryphiswaldense* MSR-1 was cultivated with the same Co, Mn and Zn mixture at the same concentration (see Materials and Methods). Three replicates were prepared for each condition.

Fig. 4 shows representative transmission electron microscopy images of biological magnetite synthesized by MTB (Figs. 4A and 4B) and abiotic magnetite nanoparticles synthesized via co-precipitation of Fe(II) and Fe(III) (Fig. 4C). To confirm the crystal phase purity of magnetite, both samples were characterized with X-ray diffraction (XRD) as presented in Fig. 5A (see Fig. S1 for XRD comparison of AMB-1 and MSR-1). X-ray diffraction showed similar peaks for all samples which are consistent with magnetite as the sole crystal phase contained in the samples. We note the abiotic sample has broader peaks due to the smaller and more dispersed crystallite sizes. Due to the nature of the co-precipitation synthesis, which does not use any surface protecting ligands, the aggregation of nanoparticles is inevitable (Fig. 4C) and thus renders it difficult to measure individual particle sizes. Therefore, XRD measurement and peak refinement yielded mean crystal sizes of about 12 and 32 nm for abiotic and biological magnetite, respectively (Table S3), though the range of particle sizes is wider in the case of biological formation. The oxidation state and coordination of Fe, Mn, Co and Zn in magnetite was determined using X-ray absorption spectroscopy (XAS). Iron K-edge XAS spectra in Figs. 5B and 5C, presented as *k*-space and R-space, show corresponding post-edge XAFS oscillations that overall match in phase, though small deviations are noticed for the abiotic sample. We attribute this to the high amount of small nanoparticles in the synthetic product (see Fig. 4C) where higher surface area to volume can shift the average scattering distances for Fe-O and Fe-Fe bonds. This difference is reflected in the EXAFS refinement of the abiotic sample (see. Fig. S2 and Table S4) where the bond distances are slightly longer and the Fe-O scattering contributions in R-space are more dominant, again reflecting the smaller particle sizes.

In both abiotic and MSR-1 cases, the magnetite samples were recovered and purified (see Materials and Methods), and their content in Fe, Co, Mn and Zn was measured using HR-ICP-MS. D^X coefficients were then determined by also analyzing the residual solution corresponding to the precipitation solution or MSR-1 growth medium. These results, given in Table S6, confirm our previous findings with D^X values highly similar or identical to those previously obtained within analytical uncertainties (Fig. 1). They further demonstrate enhanced incorporation of Co, Mn and Zn in magnetite and suggest that bacterial element screening is universal to MTB and not specific to strain type. Indeed, incorporation of Co, Cu, Mn, Ni and Zn occurs at thermodynamic equilibrium.[16] Consequently, trace and minor element incorporation do not occur at thermodynamic equilibrium in MTB, which further points to the biological control exerted by the bacteria over element transfer from the external solution to magnetite. We demonstrate below that crystal-chemical mechanisms specifically stabilizing 3d metals in the magnetite lattice correspond to crystal field effects.

Crystal field constraints on element incorporation into magnetite and coordination of 3d metals in magnetite

Elements from the first series of transition metals, including Fe, possess unfilled 3d orbitals in at least one of their oxidation sates.[25] The two sets of 3d orbitals, namely t_{2g} (*i.e.*, d_{xy}, d_{xz}, d_{yz}) and e_g (*i.e.*, d_{z^2} and $d_{x^2-y^2}$), have different geometries with the electronegative charge pointing in distinct directions. In octahedral configuration, electrons from e_g orbitals directly face the negatively charged oxygen, which maximizes the electric repulsion and thus corresponds to more energetic configurations.[25] The opposite case is observed in tetrahedral coordination. The origin and consequences of these electrostatic interactions on the energy levels of 3d orbitals is described by the crystal field theory.[25] For each element of a given valence, the crystal field stabilization energy (CFSE) was documented by McClure in octahedral and tetrahedral coordination.[26] The partitioning of Cr(II), Cr(III), Mn(II), Co(II), Ni(II), Cu(II) and Zn(II) during abiotic magnetite precipitation was modeled from their CFSE (values taken from McClure[26]) for both coordination configurations (Fig. S3). No clear correlation between $\log D^X$ and CFSE values was observed, suggesting that coordination and/or valence of doping elements are not as expected. This needed to be confirmed to determine whether crystal field effects control the incorporation of 3d metals in magnetite.

We determined the coordination and valence of Co, Mn and Zn using XAS in both abiotic and biological magnetite. The X-ray absorption near-edge structure (XANES) spectra along with references are presented in Fig. 6. Abiotic syntheses and MSR-1 cultures were performed in the presence of Co(II), Mn(II) and Zn(II) under the same experimental mixed-doping conditions. The coordination of Co, Mn and Zn has already been extensively characterized in abiotic magnetite as well as in biological magnetite produced by AMB-1 and MSR-1.[21,27–31] Therefore, this work aimed to concomitantly determine Co, Mn and Zn local structure and partition coefficients, and establish whether their incorporation can be explained by the energy level of their unfilled 3d orbitals. MSR-1 was selected for these additional experimental characterizations in order to further assess the specific behaviors of Co, Mn and Zn in MTB and evaluate their biological relevance. The D^X values corresponding to abiotic precipitation were similar to those previously obtained (see Fig. S4, Tables S1 and S6), but D^X values obtained from MSR-1 were higher than those initially obtained from AMB-1 (Fig. S4, Tables S2 and S6). Such discrepancy can be explained by the magnetite yield and intracellular Fe content in the two strains, as MSR-1 is known to incorporate more iron than AMB-1 under standard growth conditions used in the present contribution.[32] An increased mass of magnetite

increases the total mass of trace elements contained in magnetite, which in turn decreases the concentrations of trace elements in the residual medium and lead to an increase of D^X. We thus calculated partition coefficients of Mn, Co and Zn normalized to Fe ($D^{X/Fe}$) to compare values obtained from AMB-1 and MSR-1, and obtained similar results in both strains (Table S7) demonstrating that Co, Mn and Zn are highly similarly processed in AMB-1 and MSR-1.

Abiotic and biological magnetite samples were measured with XAS in powdered form at the respective dopant K-edges to confirm the valence and site occupancy of doped metals in magnetite. Due to the dopant-level concentration of each metal in magnetite, fluorescence detection was employed to collect XAS spectra. In the case of Co for abiotic magnetite nanoparticles, the fluorescence signal was too weak to collect usable spectra, which is understandable given the ten-fold lower Co concentration abiotic in magnetite relative to Mn and Zn (see Table S6). Nevertheless, from similar previous characterizations of Co-ferrite nanoparticles ($Co_xFe_{3-x}O_4$) prepared via different synthetic methods, Co is well known to occupy mainly octahedral sites[33,34] and was used forth in the CFSE calculation.

K-edge XAS for Mn-doped abiotic magnetite (Fig. 6A) has near-edge structural features that resemble a $Mn_{0.5}Fe_{2.5}O_4$ reference (where Mn is a mixture of Mn(II) located in tetrahedral sites and Mn(III) in octahedral sites).[35–37] Comparison with Mn-based oxides shows an oxidation state between Mn(II) and Mn(III) but closer to MnO. This is reflected by the position of the main rising edge (Fig. S5). Weaker pre-edge and post-edge features (6562 eV) potentially originate from the dilute and mixed nature of the dopant metal in the magnetite lattice compared to the Mn-ferrite reference. Interestingly, it was found than Mn K-edge XANES of our sample well matched Mn-ferrite nanocrystals prepared in the stoichiometry of the mineral jacobsite ($MnFe_2O_4$).[38] This reference (called $MnFe_2O_4$) is included for comparison in Fig. 6A. Here, similar edge position and near-edge features confirms comparable local environments for Mn, which was ascribed to be partially oxidized Mn(II) in 80% tetrahedral sites (*i.e.*, having 0.2 degree of inversion). Since the extended X-ray absorption fine structure (EXAFS) region is too noisy to fit scattering paths for structural information, *ab initio* simulations of the Mn K-edge XANES for tetrahedral and octahedral Mn substitutions in magnetite (Fig. S6) provided another perspective. The relative energy positions of near-edge absorption features for $Mn_{0.5}Fe_{2.5}O_4$ and $MnFe_2O_4$ references match better with tetrahedral coordination from the simulated XANES.

Zinc K-edge XANES for Zn-doped abiotic magnetite (Fig. 6C) has poorly defined near-edge features and very weak EXAFS. When compared with a Zn-ferrite reference, known to have a normal spinel crystal structure with Zn(II) occupying tetrahedral sites, the width and positioning of the XANES aligns well but clear near-edge features are less apparent.

Additionally, an unexpected near-edge feature that did not match with any of our reference materials. Based on the energy position of this feature, Zn metal contamination from the sample holder is suspected. Indeed, linear combination fitting revealed a best fit of 39% Zn metal, 36% Zn(II)-histadine complex and 25% $ZnFe_2O_4$ with R-factor = 0.0076. Without contribution from the sample holder, this translates to 59% Zn(II)-histadine and 41% $ZnFe_2O_4$. We note that histadine residues were not present in the reaction mixture. Nevertheless, due to the similarity in electronic structure of N and O, and their photoelectron backscattering properties, we attribute a portion of the Zn cations to be in molecular complex-like environments while the remaining Zn cations incorporate into magnetite as Zn-ferrite spinel.

Higher quality data was obtained for biological magnetite since dopants were found to be in higher concentration than in the abiotic samples, at least partially due to the high initial concentrations used in the bacterial growth media (Table S6). Cobalt K-edge XANES for Co-doped biological magnetite highly resembles that of a $CoFe_2O_4$ reference (Fig. 6B and Fig. S7), given the identical energies of distinctive near-edge features. From known crystal structure of Co-ferrite nanoparticles,[39,40] Co mainly occupies octahedral sites in magnetite in line with previous work on both AMB-1 and MSR-1 strains.[27,30,31] Manganese K-edge XANES of Mn-doped biological magnetite is again similar to the $Mn_{0.5}Fe_{2.5}O_4$ reference (Fig. 6A), with peak positions and their relative intensities even more comparable. The higher data quality for this sample afforded supplemental EXAFS information and a well-resolved pre-edge region. EXAFS fitting yielded a Mn-O coordination number of 4.1 ± 0.6 and a bond distance of 202 ± 2 pm (Fig. S8 and Table S8), both suggesting a tetrahedral environment for Mn dopants is likely, consistent with another recent study.[28] Nevertheless, a small contribution of Mn-Fe single scattering from Mn in octahedral sites (coordination number of 1.9 ± 0.6 and bond distance 296 ± 2 pm] was found to complete EXAFS fitting of Mn-O and Mn-Fe (coordination number of 15 ± 2 and bond distance 352 ± 5 pm) scattering from Mn in tetrahedral sites. This further confirms a partial +3 valence state of the dopant and moreover, mainly tetrahedral coordination of Mn.

Distinct Zn K-edge XANES features are more prominent for Zn-doped biological magnetite than that for the abiotic case, with near-edge features resembling a Zn-ferrite reference material (Fig. 6C). From linear combination fitting, we obtain a best fit of 64% $ZnFe_2O_4$, 18% Zn-citrate and 18% Zn metal (sample holder contamination) with R-factor = 0.0026 (Fig. S9). The smaller contribution from Zn-citrate could suggest partial octahedral coordination in addition to the tetrahedral coordination expected from Zn-ferrite. However, EXAFS fitting of Zn-O path yielded a coordination number of 4 ± 1 and bond distance of 205 ± 2 pm confirming Zn mainly

occupy tetrahedral sites (Fig. S8 and Table S8). In our case, we note a high incorporation of Zn into MSR-1 magnetite as $ZnFe_2O_4$ from doping bacteria growth media with Zn(II), whereas another study found more ZnO than $ZnFe_2O_4$.[28]

Using the experimentally determined coordination and valence of Mn, Co and Zn, a corrected CFSE was calculated. As mentioned above, Mn in abiotic magnetite showed mixed +2/+3 valence. The rising edge position (determined from the first derivative maximum of the main absorption edge) was shifted towards higher values when compared to $Mn_{0.5}Fe_{2.5}O_4$. This indicates more oxidized Mn in the abiotic magnetite samples than in the measured Mn-ferrite reference, which has been shown to contain 25% Mn(III) and 75% Mn(II),[35–37,41] while the biological magnetite overlapped the Mn-ferrite reference which suggests a similar valence for Mn. Therefore, based on the shift of the absorption edge position, the Mn(III) / Mn_{total} ratios in the abiotic and biologic magnetite were taken as 0.3 (*i.e.*, higher than Mn-ferrite reference) and 0.25 (*i.e.*, similar to Mn-ferrite reference), respectively. Zinc coordination was considered to be 60% octahedral/40% tetrahedral in the abiotic magnetite, and 20% octahedral/80% tetrahedral in the biological nanoparticles based on the fitting results. Finally, Co was considered to mainly occupy octahedral sites based on the extensive literature[42,43] that is consistent with present Co-doped MSR-1 magnetite. Measured partition coefficients represented against XAS-corrected CFSE are shown in Fig. 7. In the abiotic case, $\log D^X$ values showed a weak linear relationship with CFSE (correlation coefficient of 0.87), while biological $\log D^X$ showed almost constant values with no correlation with CFSE (correlation coefficient of 0.006) (Fig. 7A). To take into account crystal field controls independently of lattice strain mechanisms, the measured partition coefficients in abiotic nanoparticles were normalized to the D^X predicted from lattice strain theory (Eq. 2 and Fig. 1). The results are presented in Fig. 7B and show a stronger linear correlation between the trace element stabilization and the corrected CFSE (correlation coefficient of 0.99). Our results thus demonstrate the importance of taking into account the actual coordination of trace 3d metals in magnetite since their incorporation is controlled by crystal field mechanisms.

Conclusion

The present contribution establishes an experimental and theoretical framework that can predict the behavior of trace and minor cations during synthetic magnetite formation based on their size, valence and unfilled 3d orbitals. It also helps elucidate the screening effect MTB have on biological magnetite formation. Beyond the geobiological interests for the identification of ancient terrestrial and extra-terrestrial life, our work has significant

implications for nanotechnological applications of biological and/or abiotic nanoparticles of magnetite. Deliberate doping of trace and minor elements has been carried out to optimize magnetite nanoparticle composition for dedicated applications, including doping of Co and Zn that increase the efficiency of magnetite's magnetic properties for cancer treatment using hyperthermia,[8,9,44] as well as its capacity of organic pollutant remediation and (bio)remediation of contaminated water.[45–47] The appropriateness of doped magnetite nanomaterials with tailored properties (*e.g.*, magnetism) for future applications will be further evaluated with our methodology by identifying the different outcomes of dopant composition via abiotic or biological synthesis.

Materials and Methods

Magnetite abiotic synthesis

Production of abiotic magnetite nanoparticles was performed using a titration device as already described.[48] An Fe chloride mixture ([Fe(II)Cl_2] = 0.33 M and [Fe(III)Cl_3] = 0.66 M) was added to a NaOH solution (pH = 11) at room-temperature. The decrease of pH associated with the release of protons during magnetite precipitation was compensated by adding additional NaOH solution (1 M) to keep the pH constant throughout the experiment. All doping elements were mixed in the Fe solution and added at similar concentrations (100 ppb for each element from dissolution of chloride salts purchased from Sigma-Aldrich). The Fe mixture, NaOH solution, and the magnetite precipitation solution were kept under constant anoxic conditions by flushing N_2 to prevent Fe(II) oxidation. Magnetite samples were then recovered by centrifugation (8 000 rpm for 15 min), rinsed two times with Milli-Q water and dried in a desiccator. All samples were kept under anoxic conditions before XAS analyses. Electron microscopy revealed nanoparticles with size and shape similar to previous works using the same co-precipitation method for magnetite production.[10,22]

Bacterial cultures and magnetite purification

Procedures for AMB-1 cultivation are detailed in previous work.[10] Two culturing methods were used for AMB-1 (batch and fermentor cultures) to assess the biological variability induced by different culture conditions. The size of nanoparticles produced by MSR-1 is in the range of published works on both AMB-1 and MSR-1 strains.[49–51] MSR-1 magnetite observed with electron microscopy was similar in size (Table S3) and shape to standard MSR-1 cultures as previously observed.[32] Because MTB magnetite is strongly depleted in dopant elements compared to its abiotic counterpart,[10] Mn, Co and Zn were added at higher concentration to

maximize their incorporation into MSR-1 magnetite for XAS measurements (see Fig. S10 for doping trials with Cu and Ni). Doping elements were added at similar concentrations (33 μM for each element in the mixed-element condition, and 100 μM for single-doped samples from dissolution of chloride salts purchased from Sigma-Aldrich) in MSR-1 growth medium. They did not induce toxicity for the bacteria, as shown by similar cell densities in doped cultures when compared to bacteria cultivated with no doping elements (Table S9). MSR-1 magnetite was then extracted for XAS and HR-ICP-MS analyses: MSR-1 bacteria were lysed using a French Press (3 runs at 7 000 kPa), recovered with a magnet, and purified with an EDTA-Triton-SDS preparation following a previously described procedure.[10] Complete removal of the magnetosome membrane using this protocol was previously confirmed from electron microscopy (no membrane features after purification) and energy dispersive X-ray spectroscopy (no detectable phosphorous and nitrogen after purification, which are elements contained in organic matter and absent from magnetite). This was also confirmed for our biological magnetite samples, which showed no residual membrane after purification (Fig. 4). Finally, all magnetite samples were leached using an EDTA solution for 20 minutes to remove elements adsorbed on the magnetite surface but not incorporated into the crystal lattice.[10] Such methodology was shown not to dissolve magnetite.[10] The partition coefficients normalized to iron obtained in this work were identical (within analytical uncertainty) to the ones previously obtained in the initial study establishing the purification protocol, further demonstrating that magnetite samples were efficiently purified.[10]

Transmission electron microscopy

Abiotic magnetite nanoparticles and MSR-1 bacteria were deposited on carbon-coated copper grids for electron microscopy characterizations. MSR-1 grids were rinsed using Milli-Q water to remove salts precipitated from the growth medium. Samples were then observed with a FEI Tecnai G2 Biotwin microscope operating at 100 kV. The size of magnetite particles produced by MSR-1 was measured with the ImageJ software. The size of abiotic magnetite nanoparticles could not be measured reliably from electron microscopy due to agglomeration, and was instead determined from X-ray diffraction (see below).

Selection of trace and minor elements

Four elements (B, Ca, K, Mg) from the initial work[10] were excluded for the present work: B and K are contained in the glassware (borosilicates) used for the preparation and storage of

samples, and thus contaminate the magnetite and solution samples, while only one replicate could be obtained in the case of Ca and Mg.

Determination of element oxidation state in solution and magnetite

The oxidation state of all doping trace and minor elements in precipitation solutions was determined at the pH / E_h conditions representative of the abiotic precipitation solution and the proposed magnetosome internal solution[18] with the geochemical code CHESS[52] using the THERMODDEM[53] database. Because Fe(II) is found in octahedral sites in magnetite, all divalent cations were considered as occupying octahedral sites in magnetite. Similarly, half of Fe(III) is present in octahedral sites magnetite, the other half being contained in tetrahedral sites. We thus considered trivalent cations to be incorporated in both 6- (50%) and 4-coordination (50%).

Prediction of trace and minor element partition coefficients from lattice strain theory

The distribution of D^X values for an isovalent series of elements can be described by ref.[15]:

$$D^X = D_{n+}^{0(M)} \times exp\left\{\frac{-4\pi N_A E^M \left[\frac{1}{2}r^{0(M)}\left(r^X - r^{0(M)}\right)^2 + \frac{1}{3}\left(r^X - r^{0(M)}\right)^3\right]}{RT}\right\} \quad (2)$$

With $D_{n+}^{0(M)}$ the partition coefficient for a fictive element with $r^X = r_{n+}^{0(M)}$ and causing no elastic strain (*i.e.* strain-compensated D^X), E_{n+}^M the lattice strain parameter describing the Young's Modulus (in GPa) of the site M, N_A the Avogadro's number, R the perfect gas constant, and T the temperature in Kelvin. Similarly, heterovalent cation substitution entail excess electric charge accommodated by the crystal lattice that will also translate into a penalty in energy for element incorporation[15]:

$$D_{n+}^{0(M)} = D^{00(M)} \times exp\left\{\frac{-N_A e^2 \left(Z^X - Z^{0(M)}\right)^2}{(2\varepsilon\rho RT)}\right\} \quad (3)$$

Where $D^{00(M)}$ is the strain-compensated partition coefficient for a fictive ion causing no electrostatic charging (*i.e.*, homovalent substitution), e the electron charge, ρ the radius of the region over which the excess charge is distributed, ε the dielectric constant of that region, and Z^X and $Z^{0(M)}$ the ionic charge and the optimum ionic charge at the site M, respectively.

The parameters used for the calculation of predicted partition coefficients using Eq. 2 ($D^{0(M)}_{n+}$, $r^{0(M)}_{n+}$, and E^M_{n+}) are given in Table S5. Selected Young's modulus range between 90 and 430

GPa , which is in good agreement with the range of published values for macrocrystals and nanoparticles of magnetite.[54–56] Higher variability in E^{M}_{n+} than that observed here for magnetite has already been reported in many mineral phases, including plagioclase, diopside, augite, anorthite, albite, diopside or fluorite.[57,58] Such variability is related to the ion charge and the cation – oxygen distance.[15] In the case of magnetite, it can also be explained by the variability induced by the two lattice sites under consideration (tetrahedral and octahedral). For Eq. 3, a dielectric constant (ε) of 55 and a lattice region with a radius (ρ) of 9 nm were considered. Such values correspond to published ε for magnetite.[59,60] Due to the agglomerated nature of abiotic magnetite samples, it was impossible to assess the particle size from electron microscopy. XRD peak fitting indicated a mean radius of 6 nm for abiotic nanoparticles. However it is known to generate lower (up to 50 %) values than direct observation from electron microscopy.[22] Given the discrepancy between these two techniques, we consider our theoretical value of 9 nm to be compatible with the size of our abiotic magnetite samples.

We note that the partition coefficient D^{X} is expressed differently from other publications of our group.[10,16] Specifically, it is not normalized to iron (except for the AMB-1/MSR-1 comparison, see section "Crystal field constraints on element incorporation into magnetite and coordination of 3d metals in magnetite" for details) to determine the values of $D^{0(M)}_{n+}$ and $D^{00(M)}$ coefficients).

Inductively Coupled Plasma – Mass Spectrometry (ICP-MS) analyses

The concentrations of Fe, Mn, Co and Zn in the abiotic and MSR-1 magnetite nanoparticles (samples only from the metal mixture culture were used), in the residual precipitation solution and in the residual bacterial growth media were determined using a Perkin Elmer NexIon 300X mass spectrometer (collision mode configuration with a Rh103 internal standard) at the *Centre Européen de Recherche et d'Enseignement en Géosciences de l'Environnement* (CEREGE Aix-en-Provence, France). Three replicates were performed for each experimental condition.

X-ray diffraction (XRD)

X-ray diffraction measurements were performed at the μSpot beamline at the BESSY II facility (Helmholtz Zentrum für Materialien und Energie, Berlin, Germany).[61] Measurements were carried out using a B4C/Mo Multilayer (2 nm period) monochromator and an energy of 15 keV. A sequence of pinholes was used to select 100x100 μm^2 spot size. The data was normalized on primary beam intensity and the background was subtracted. Transmission through the sample was calculated from an X-ray fluorescence signal collected from a lead beamstop using

RAYSPEC Sirius SD-E65133-BE-INC detector equipped with an 8 μm beryllium window, where the primary beam intensity was monitored using an ion chamber. Diffraction data were collected by an Eiger 9M detector with 75x75 μm^2 pixel area. Further data processing and reduction was done using the directly programmable data analysis kit (DPDAK).[62] Diffraction patterns were radially integrated and the scattered intensity I(Q) was calculated as a function of the momentum transfer Q, defined as

$$Q = \frac{\cdots}{\lambda} sin(\frac{\cdot}{2}) \quad (4)$$

with λ and θ the photon wavelength and the scattering angle, respectively. Sample to detector distance was set to 189 mm and calibrated by using quartz powder (NIST, standard reference material 1878a). Determination of peak position and particle size was performed following established methodology with an in-house python-based script exploiting Scipy library. Fits were performed by assuming a Lorentzian distribution and by taking into account experimental errors and instrumental broadening (Fig. S11).

X-ray Absorption Spectroscopy (XAS)

The abiotic and biological magnetite samples were measured under cryogenic conditions in powdered form. To prepare the samples for measurement, the purified abiotic and biological magnetite nanoparticles were spread onto Kapton tape and folded to seal the sample. The samples were kept frozen during storage, shipment and measurement. Principal data was collected at the I20-Scanning beamline (Diamond Light Source, Didcot, UK). Preliminary XAS data (additional Fe, Ni and Cu K-edge spectra) was collected at the Sector BM-20 beamline (Advanced Photon Source, Argonne National Laboratory, IL, USA). Additional reference materials were acquired and energy calibrated for comparison with abiotic and biological samples. Due to the dilute nature of dopant metals, fluorescence detection was employed to collect XAS spectra. Several scans were collected and averaged to produce the spectra presented in this work. XAS of reference foils for Mn, Co and Zn were simultaneously collected downstream via ionization chambers for energy calibration. Athena and WinXAS programs were used for background subtraction, energy calibration, normalization and transformation to FT-EXAFS spectra. Athena was implemented for linear combination fitting and WinXAS for refined EXAFS fitting. The computational package FEFF8.2 was employed to simulate scattering paths for EXAFS fitting and to simulate Mn K-edge XANES of Mn in octahedral and tetrahedral lattice sites in magnetite. Reported errors in EXAFS fitting results were

computed from off-diagonal elements of the correlation matrix, which were weighted by the square root of the reduced chi-squared values obtained from each simulated fit. The amount of experimental noise was also taken into consideration for each Fourier transformed R-space spectrum from 15-25 Å.

Acknowledgements

MA is supported by a grant through the *Fondation pour la Recherche Médicale* (ARF201909009123). DMC acknowledges research funding through a European Union Marie-Skłodowska Curie Action International Fellowship (MSCA-IF Project 797431: BioNanoMagnets) and from a CNRS starting grant. CLS@APS facilities (Sector 20-BM) at the Advanced Photon Source (APS) are supported by the U.S. Department of Energy (DOE), NSERC Canada, the University of Washington, the Canadian Light Source (CLS), and the APS. Use of the APS is supported by the DOE under Contract No. DE-AC02−06CH11357. We acknowledge Diamond Light Source for beamtime on I20-scanning under proposal SP25495. We thank beamline scientists Michael Pape (APS) for technical assistance during beamtimes. The groups of Thomas N. Stokes, Daniela Carta, Alicia Muela and M. Luisa Fdez-Gubieda are thanked for sharing XAS data on ferrite references. We thank Bernard Angeletti and Jean-Paul Ambrosi from the *Centre Européen de Recherche et d'Enseignement des Géosciences de l'Environnement (*Aix-en-Provence, France*)* for assistance with the mass spectrometry measurements. We thank Lucas Kuhrts for providing additional reference XRD diffractogram of magnetite and Paul N. Duchesne for constructive feedback and comments on the manuscript.

Associated Content

Supporting Information is available free of charge at https://pubs.acs.org/doi/10.1021/acsnano… The file contains additional X-ray diffraction and X-ray absorption spectroscopy data for abiotic and biological magnetite samples, plots and tabulated values of calculated partition coefficients, massic concentration of elements from ICP-MS measurements, particle size measurements, EXAFS fitting results, ideal radii and Young's modulus values for lattice strain calculations and results from dopant metal tolerance study.

This manuscript was initially deposited on a pre-print server and can be found with the following information: Matthieu Amor, Damien Faivre, Daniel M. Chevrier, Crystal-chemical and biological controls of trace and minor element incorporation into magnetite nanocrystals. 2021, ChemRxiv. https://chemrxiv.org/engage/chemrxiv/article-details/6177bd06913a742b636afc83 (accessed December 16, 2022).

622

References

(1) Usman, M.; Byrne, J. M.; Chaudhary, A.; Orsetti, S.; Hanna, K.; Ruby, C.; Kappler, A.; Haderlein, S. B. Magnetite and Green Rust: Synthesis, Properties, and Environmental Applications of Mixed-Valent Iron Minerals. *Chem. Rev.* **2018**, *118* (7), 3251–3304. https://doi.org/10.1021/acs.chemrev.7b00224.

(2) Uebe, R.; Schüler, D. Magnetosome Biogenesis in Magnetotactic Bacteria. *Nat. Rev. Microbiol.* **2016**, *14* (10), 621–637. https://doi.org/10.1038/nrmicro.2016.99.

(3) Lin, W.; Paterson, G. A.; Zhu, Q.; Wang, Y.; Kopylova, E.; Li, Y.; Knight, R.; Bazylinski, D. A.; Zhu, R.; Kirschvink, J. L.; Pan, Y. Origin of Microbial Biomineralization and Magnetotaxis during the Archean. *Proc. Natl. Acad. Sci. U. S. A.* **2017**, *114* (9), 2171–2176. https://doi.org/10.1073/pnas.1614654114.

(4) Amor, M.; Mathon, F. P.; Monteil, C. L.; Busigny, V.; Lefevre, C. T. Iron-Biomineralizing Organelle in Magnetotactic Bacteria: Function, Synthesis and Preservation in Ancient Rock Samples. *Environ. Microbiol.* **2020**, *22* (9), 3611–3632. https://doi.org/10.1111/1462-2920.15098.

(5) Plan Sangnier, A.; Preveral, S.; Curcio, A.; K A Silva, A.; Lefèvre, C. T.; Pignol, D.; Lalatonne, Y.; Wilhelm, C. Targeted Thermal Therapy with Genetically Engineered Magnetite Magnetosomes@RGD: Photothermia Is Far More Efficient than Magnetic Hyperthermia. *J Control Release* **2018**, *279*, 271–281. https://doi.org/10.1016/j.jconrel.2018.04.036.

(6) Felfoul, O.; Mohammadi, M.; Taherkhani, S.; de Lanauze, D.; Xu, Y. Z.; Loghin, D.; Essa, S.; Jancik, S.; Houle, D.; Lafleur, M.; Gaboury, L.; Tabrizian, M.; Kaou, N.; Atkin, M.; Vuong, T.; Batist, G.; Beauchemin, N.; Radzioch, D.; Martel, S. Magneto-Aerotactic Bacteria Deliver Drug-Containing Nanoliposomes to Tumour Hypoxic Regions. *Nat. Nanotechnol.* **2016**, *11* (11), 941–947. https://doi.org/10.1038/NNANO.2016.137.

(7) Zingsem, B. W.; Feggeler, T.; Terwey, A.; Ghaisari, S.; Spoddig, D.; Faivre, D.; Meckenstock, R.; Farle, M.; Winklhofer, M. Biologically Encoded Magnonics. *Nature Communications* **2019**, *10* (1), 4345. https://doi.org/10.1038/s41467-019-12219-0.

(8) Byrne, J. M.; Coker, V. S.; Moise, S.; Wincott, P. L.; Vaughan, D. J.; Tuna, F.; Arenholz, E.; van der Laan, G.; Pattrick, R. A. D.; Lloyd, J. R.; Telling, N. D. Controlled Cobalt Doping in Biogenic Magnetite Nanoparticles. *Journal of The Royal Society Interface* **2013**, *10* (83), 20130134. https://doi.org/10.1098/rsif.2013.0134.

(9) Byrne, J. M.; Coker, V. S.; Cespedes, E.; Wincott, P. L.; Vaughan, D. J.; Pattrick, R. A. D.; Laan, G. van der; Arenholz, E.; Tuna, F.; Bencsik, M.; Lloyd, J. R.; Telling, N. D. Biosynthesis of Zinc Substituted Magnetite Nanoparticles with Enhanced Magnetic Properties. *Advanced Functional Materials* **2014**, *24* (17), 2518–2529. https://doi.org/10.1002/adfm.201303230.

(10) Amor, M.; Busigny, V.; Durand-Dubief, M.; Tharaud, M.; Ona-Nguema, G.; Gélabert, A.; Alphandéry, E.; Menguy, N.; Benedetti, M. F.; Chebbi, I.; Guyot, F. Chemical Signature of Magnetotactic Bacteria. *Proc. Natl. Acad. Sci. U. S. A.* **2015**, *112* (6), 1699–1703. https://doi.org/10.1073/pnas.1414112112.

(11) Thomas-Keprta, K. L.; Bazylinski, D. A.; Kirschvink, J. L.; Clemett, S. J.; McKay, D. S.; Wentworth, S. J.; Vali, H.; Gibson, E. K.; Romanek, C. S. Elongated Prismatic Magnetite Crystals in ALH84001 Carbonate Globules: Potential Martian Magnetofossils. *Geochim. Cosmochim. Acta* **2000**, *64* (23), 4049–4081. https://doi.org/10.1016/S0016-7037(00)00481-6.

(12) Thomas-Keprta, K. L.; Clemett, S. J.; McKay, D. S.; Gibson, E. K.; Wentworth, S. J. Origins of Magnetite Nanocrystals in Martian Meteorite ALH84001. *Geochim. Cosmochim.*

Acta **2009**, *73* (21), 6631–6677. https://doi.org/10.1016/j.gca.2009.05.064.
(13) Golden, D. C.; Ming, D. W.; Schwandt, C. S.; Lauer, H. V.; Socki, R. A.; Morris, R. V.; Lofgren, G. E.; McKay, G. A. A Simple Inorganic Process for Formation of Carbonates, Magnetite, and Sulfides in Martian Meteorite ALH84001. *Am. Miner.* **2001**, *86* (3), 370–375.
(14) Jimenez-Lopez, C.; Rodriguez-Navarro, C.; Rodriguez-Navarro, A.; Perez-Gonzalez, T.; Bazylinski, D. A.; Lauer, H. V.; Romanek, C. S. Signatures in Magnetites Formed by (Ca,Mg,Fe)CO3 Thermal Decomposition: Terrestrial and Extraterrestrial Implications. *Geochim. Cosmochim. Acta* **2012**, *87*, 69–80. https://doi.org/10.1016/j.gca.2012.03.028.
(15) Blundy, J.; Wood, B. Partitioning of Trace Elements between Crystals and Melts. *Earth Planet. Sci. Lett.* **2003**, *210* (3–4), 383–397. https://doi.org/10.1016/S0012-821X(03)00129-8.
(16) Amor, M.; Faivre, D.; Corvisier, J.; Tharaud, M.; Busigny, V.; Komeili, A.; Guyot, F. Defining Local Chemical Conditions in Magnetosomes of Magnetotactic Bacteria. *J. Phys. Chem. B* **2022**, *126* (14), 2677–2687. https://doi.org/10.1021/acs.jpcb.2c00752.
(17) Ona-Nguema, G.; Morin, G.; Wang, Y.; Foster, A. L.; Juillot, F.; Calas, G.; Brown, G. E. XANES Evidence for Rapid Arsenic(III) Oxidation at Magnetite and Ferrihydrite Surfaces by Dissolved O-2 via Fe2+-Mediated Reactions. *Environ. Sci. Technol.* **2010**, *44* (14), 5416–5422. https://doi.org/10.1021/es1000616.
(18) Eguchi, Y.; Fukumori, Y.; Taoka, A. Measuring Magnetosomal PH of the Magnetotactic Bacterium Magnetospirillum Magneticum AMB-1 Using PH-Sensitive Fluorescent Proteins. *Biosci. Biotechnol. Biochem.* **2018**, *82* (7), 1243–1251. https://doi.org/10.1080/09168451.2018.1451739.
(19) Hsueh, Y.-H.; Lin, K.-S.; Ke, W.-J.; Hsieh, C.-T.; Chiang, C.-L.; Tzou, D.-Y.; Liu, S.-T. The Antimicrobial Properties of Silver Nanoparticles in Bacillus Subtilis Are Mediated by Released Ag+ Ions. *PLOS ONE* **2015**, *10* (12), e0144306. https://doi.org/10.1371/journal.pone.0144306.
(20) Komeili, A. Molecular Mechanisms of Compartmentalization and Biomineralization in Magnetotactic Bacteria. *Fems Microbiol. Rev.* **2012**, *36* (1), 232–255. https://doi.org/10.1111/j.1574-6976.2011.00315.x.
(21) Marcano, L.; Orue, I.; García-Prieto, A.; Abrudan, R.; Alonso, J.; Fernández Barquín, L.; Valencia, S.; Muela, A.; Fdez-Gubieda, M. L. Controlled Magnetic Anisotropy in Single Domain Mn-Doped Biosynthesized Nanoparticles. *J. Phys. Chem. C* **2020**, *124* (41), 22827–22838. https://doi.org/10.1021/acs.jpcc.0c07018.
(22) Kuhrts, L.; Macías-Sánchez, E.; Tarakina, N. V.; Hirt, A. M.; Faivre, D. Shaping Magnetite with Poly-l-Arginine and PH: From Small Single Crystals to Large Mesocrystals. *J. Phys. Chem. Lett.* **2019**, *10* (18), 5514–5518. https://doi.org/10.1021/acs.jpclett.9b01771.
(23) Kuhrts, L.; Prévost, S.; Chevrier, D. M.; Pekker, P.; Spaeker, O.; Egglseder, M.; Baumgartner, J.; Pósfai, M.; Faivre, D. Wettability of Magnetite Nanoparticles Guides Growth from Stabilized Amorphous Ferrihydrite. *J. Am. Chem. Soc.* **2021**, *143* (29), 10963–10969. https://doi.org/10.1021/jacs.1c02687.
(24) Baumgartner, J.; Bertinetti, L.; Widdrat, M.; Hirt, A. M.; Faivre, D. Formation of Magnetite Nanoparticles at Low Temperature: From Superparamagnetic to Stable Single Domain Particles. *PLOS ONE* **2013**, *8* (3), e57070. https://doi.org/10.1371/journal.pone.0057070.
(25) Burns, R. G. *Mineralogical Applications of Crystal Field Theory*; Cambridge University Press, 1993.
(26) McClure, D. S. The Distribution of Transition Metal Cations in Spinels. *Journal of Physics and Chemistry of Solids* **1957**, *3* (3), 311–317. https://doi.org/10.1016/0022-3697(57)90034-3.
(27) Marcano, L.; Muñoz, D.; Martín-Rodríguez, R.; Orue, I.; Alonso, J.; García-Prieto, A.;

Serrano, A.; Valencia, S.; Abrudan, R.; Fernández Barquín, L.; García-Arribas, A.; Muela, A.; Fdez-Gubieda, M. L. Magnetic Study of Co-Doped Magnetosome Chains. *J. Phys. Chem. C* **2018**, *122* (13), 7541–7550. https://doi.org/10.1021/acs.jpcc.8b01187.

(28) Muñoz, D.; Marcano, L.; Martín-Rodríguez, R.; Simonelli, L.; Serrano, A.; García-Prieto, A.; Fdez-Gubieda, M. L.; Muela, A. Magnetosomes Could Be Protective Shields against Metal Stress in Magnetotactic Bacteria. *Sci Rep* **2020**, *10* (1), 11430. https://doi.org/10.1038/s41598-020-68183-z.

(29) Prozorov, T.; Perez-Gonzalez, T.; Valverde-Tercedor, C.; Jimenez-Lopez, C.; Yebra-Rodriguez, A.; Körnig, A.; Faivre, D.; Mallapragada, S. K.; Howse, P. A.; Bazylinski, D. A.; Prozorov, R. Manganese Incorporation into the Magnetosome Magnetite: Magnetic Signature of Doping. *Eur. J. Mineral.* **2014**, *26* (4), 457–471. https://doi.org/10.1127/0935-1221/2014/0026-2388.

(30) Staniland, S.; Williams, W.; Telling, N.; Van der Laan, G.; Harrison, A.; Ward, B. Controlled Cobalt Doping of Magnetosomes in Vivo. *Nat. Nanotechnol.* **2008**, *3* (3), 158–162. https://doi.org/10.1038/nnano.2008.35.

(31) Li, J.; Menguy, N.; Arrio, M.-A.; Sainctavit, P.; Juhin, A.; Wang, Y.; Chen, H.; Bunau, O.; Otero, E.; Ohresser, P.; Pan, Y. Controlled Cobalt Doping in the Spinel Structure of Magnetosome Magnetite: New Evidences from Element- and Site-Specific X-Ray Magnetic Circular Dichroism Analyses. *J. R. Soc. Interface* **2016**, *13* (121), 20160355. https://doi.org/10.1098/rsif.2016.0355.

(32) Heyen, U.; Schuler, D. Growth and Magnetosome Formation by Microaerophilic Magnetospirillum Strains in an Oxygen-Controlled Fermentor. *Appl. Microbiol. Biotechnol.* **2003**, *61* (5–6), 536–544. https://doi.org/10.1007/s00253-002-1219-x.

(33) Tsvetkov, M.; Milanova, M.; Ivanova, I.; Neov, D.; Cherkezova-Zheleva, Z.; Zaharieva, J.; Abrashev, M. Phase Composition and Crystal Structure Determination of Cobalt Ferrite, Modified with Ce, Nd and Dy Ions by X-Ray and Neutron Diffraction. *Journal of Molecular Structure* **2019**, *1179*, 233–241. https://doi.org/10.1016/j.molstruc.2018.07.083.

(34) Amiri, S.; Shokrollahi, H. The Role of Cobalt Ferrite Magnetic Nanoparticles in Medical Science. *Materials Science and Engineering: C* **2013**, *33* (1), 1–8. https://doi.org/10.1016/j.msec.2012.09.003.

(35) Mazarío, E.; Mayoral, A.; Salas, E.; Menéndez, N.; Herrasti, P.; Sánchez-Marcos, J. Synthesis and Characterization of Manganese Ferrite Nanoparticles Obtained by Electrochemical/Chemical Method. *Mater. Des.* **2016**, *111*, 646–650. https://doi.org/10.1016/j.matdes.2016.09.031.

(36) Stokes, T. N.; Bromiley, G. D.; Gatta, G. D.; Rotiroti, N.; Potts, N. J.; Saunders, K. Cation Distribution and Valence in Synthetic Al–Mn–O and Fe–Mn–O Spinels under Varying Conditions. *Mineralogical Magazine* **2018**, *82* (4), 975–992. https://doi.org/10.1180/mgm.2018.109.

(37) Liang, X.; Zhong, Y.; Zhu, S.; He, H.; Yuan, P.; Zhu, J.; Jiang, Z. The Valence and Site Occupancy of Substituting Metals in Magnetite Spinel Structure Fe3−xMxO4 (M = Cr, Mn, Co and Ni) and Their Influence on Thermal Stability: An XANES and TG-DSC Investigation. *Solid State Sci.* **2013**, *15*, 115–122. https://doi.org/10.1016/j.solidstatesciences.2012.10.005.

(38) Carta, D.; Casula, M. F.; Falqui, A.; Loche, D.; Mountjoy, G.; Sangregorio, C.; Corrias, A. A Structural and Magnetic Investigation of the Inversion Degree in Ferrite Nanocrystals MFe2O4 (M = Mn, Co, Ni). *J. Phys. Chem. C* **2009**, *113* (20), 8606–8615. https://doi.org/10.1021/jp901077c.

(39) Swatsitang, E.; Phokha, S.; Hunpratub, S.; Usher, B.; Bootchanont, A.; Maensiri, S.; Chindaprasirt, P. Characterization and Magnetic Properties of Cobalt Ferrite Nanoparticles. *Journal of Alloys and Compounds* **2016**, *664*, 792–797.

https://doi.org/10.1016/j.jallcom.2015.12.230.
(40) Nakagomi, F.; da Silva, S. W.; Garg, V. K.; Oliveira, A. C.; Morais, P. C.; Franco Júnior, A.; Lima, E. C. D. The Influence of Cobalt Population on the Structural Properties of CoxFe3−xO4. *Journal of Applied Physics* **2007**, *101* (9), 09M514. https://doi.org/10.1063/1.2712821.
(41) Carta, D.; Casula, M. F.; Floris, P.; Falqui, A.; Mountjoy, G.; Boni, A.; Sangregorio, C.; Corrias, A. Synthesis and Microstructure of Manganese Ferrite Colloidal Nanocrystals. *Phys. Chem. Chem. Phys.* **2010**, *12* (19), 5074–5083. https://doi.org/10.1039/B922646J.
(42) Toksha, B. G.; Shirsath, S. E.; Mane, M. L.; Patange, S. M.; Jadhav, S. S.; Jadhav, K. M. Autocombustion High-Temperature Synthesis, Structural, and Magnetic Properties of CoCrxFe2–XO4 ($0 \leq x \leq 1.0$). *J. Phys. Chem. C* **2011**, *115* (43), 20905–20912. https://doi.org/10.1021/jp205572m.
(43) Giri, A. K.; Kirkpatrick, E. M.; Moongkhamklang, P.; Majetich, S. A.; Harris, V. G. Photomagnetism and Structure in Cobalt Ferrite Nanoparticles. *Appl. Phys. Lett.* **2002**, *80* (13), 2341–2343. https://doi.org/10.1063/1.1464661.
(44) Alphandery, E.; Carvallo, C.; Menguy, N.; Chebbi, I. Chains of Cobalt Doped Magnetosomes Extracted from AMB-1 Magnetotactic Bacteria for Application in Alternative Magnetic Field Cancer Therapy. *J. Phys. Chem. C* **2011**, *115* (24), 11920–11924. https://doi.org/10.1021/jp201274g.
(45) Fazli, A.; Khataee, A.; Brigante, M.; Mailhot, G. Cubic Cobalt and Zinc Co-Doped Magnetite Nanoparticles for Persulfate and Hydrogen Peroxide Activation towards the Effective Photodegradation of Sulfalene. *Chem. Eng. J.* **2021**, *404*, 126391. https://doi.org/10.1016/j.cej.2020.126391.
(46) Huber, F.; Schild, D.; Vitova, T.; Rothe, J.; Kirsch, R.; Schaefer, T. U(VI) Removal Kinetics in Presence of Synthetic Magnetite Nanoparticles. *Geochim. Cosmochim. Acta* **2012**, *96*, 154–173. https://doi.org/10.1016/j.gca.2012.07.019.
(47) Crean, D. E.; Coker, V. S.; van der Laan, G.; Lloyd, J. R. Engineering Biogenic Magnetite for Sustained Cr(VI) Remediation in Flow-through Systems. *Environ. Sci. Technol.* **2012**, *46* (6), 3352–3359. https://doi.org/10.1021/es2037146.
(48) Baumgartner, J.; Carillo, M. A.; Eckes, K. M.; Werner, P.; Faivre, D. Biomimetic Magnetite Formation: From Biocombinatorial Approaches to Mineralization Effects. *Langmuir* **2014**, *30* (8), 2129–2136. https://doi.org/10.1021/la404290c.
(49) Olszewska-Widdrat, A.; Schiro, G.; Reichel, V. E.; Faivre, D. Reducing Conditions Favor Magnetosome Production in Magnetospirillum Magneticum AMB-1. *Front. Microbiol.* **2019**, *10*, 582. https://doi.org/10.3389/fmicb.2019.00582.
(50) Amor, M.; Ceballos, A.; Wan, J.; Simon, C. P.; Aron, A. T.; Chang, C. J.; Hellman, F.; Komeili, A. Magnetotactic Bacteria Accumulate a Large Pool of Iron Distinct from Their Magnetite Crystals. *Appl. Environ. Microbiol.* **2020**, *86* (22), e01278-20. https://doi.org/10.1128/AEM.01278-20.
(51) Lohße, A.; Borg, S.; Raschdorf, O.; Kolinko, I.; Tompa, É.; Pósfai, M.; Faivre, D.; Baumgartner, J.; Schüler, D. Genetic Dissection of the MamAB and Mms6 Operons Reveals a Gene Set Essential for Magnetosome Biogenesis in Magnetospirillum Gryphiswaldense. *J Bacteriol* **2014**, *196* (14), 2658–2669. https://doi.org/10.1128/JB.01716-14.
(52) Van der Lee, J.; De Windt, L. CHESS Tutorial and Cookbook. Updated for Version 3.0, Manual Nr. LHM/RD/02/13.; Paris, 2002; p 116.
(53) Blanc, P.; Lassin, A.; Piantone, P.; Azaroual, M.; Jacquemet, M.; Fabbri, A.; Gaucher, E. C. Thermoddem: A Geochemical Database Focused on Low Temperature Water/Rock Interactions and Waste Materials. *Appl. Geochem.* **2012**, *27* (10), 2107–2116. https://doi.org/10.1016/j.apgeochem.2012.06.002.
(54) Chicot, D.; Mendoza, J.; Zaoui, A.; Louis, G.; Lepingle, V.; Roudet, F.; Lesage, J.

Mechanical Properties of Magnetite (Fe3O4), Hematite (Alpha-Fe2O3) and Goethite (Alpha-FeO Center Dot OH) by Instrumented Indentation and Molecular Dynamics Analysis. *Mater. Chem. Phys.* **2011**, *129* (3), 862–870. https://doi.org/10.1016/j.matchemphys.2011.05.056.

(55) Fine, M. E.; Kenney, N. T. Moduli and Internal Friction of Magnetite as Affected by the Low-Temperature Transformation. *Phys. Rev.* **1954**, *94* (6), 1573–1576. https://doi.org/10.1103/PhysRev.94.1573.

(56) Gholizadeh, A. A Comparative Study of Physical Properties in Fe3O4 Nanoparticles Prepared by Coprecipitation and Citrate Methods. *J. Am. Ceram. Soc.* **2017**, *100* (8), 3577–3588. https://doi.org/10.1111/jace.14896.

(57) Blundy, J.; Wood, B. Prediction of Crystal-Melt Partition-Coefficients from Elastic-Moduli. *Nature* **1994**, *372* (6505), 452–454. https://doi.org/10.1038/372452a0.

(58) van Hinsberg, V. J.; Migdisov, A. A.; Williams-Jones, A. E. Reading the Mineral Record of Fluid Composition from Element Partitioning. *Geology* **2010**, *38* (9), 847–850. https://doi.org/10.1130/G31112.1.

(59) Pimenov, A.; Tachos, S.; Rudolf, T.; Loidl, A.; Schrupp, D.; Sing, M.; Claessen, R.; Brabers, V. A. M. Terahertz Conductivity at the Verwey Transition in Magnetite. *Phys. Rev. B* **2005**, *72* (3), 035131. https://doi.org/10.1103/PhysRevB.72.035131.

(60) Zulfiqar; Afzal, S.; Khan, R.; Zeb, T.; Rahman, M. ur; Burhanullah; Ali, S.; Khan, G.; Rahman, Z. ur; Hussain, A. Structural, Optical, Dielectric and Magnetic Properties of PVP Coated Magnetite (Fe3O4) Nanoparticles. *J Mater Sci: Mater Electron* **2018**, *29* (23), 20040–20050. https://doi.org/10.1007/s10854-018-0134-6.

(61) Zizak, I. The MySpot Beamline at BESSY II. *Journal of large-scale research facilities JLSRF* **2016**, *2* (0), 102. https://doi.org/10.17815/jlsrf-2-113.

(62) Benecke, G.; Wagermaier, W.; Li, C.; Schwartzkopf, M.; Flucke, G.; Hoerth, R.; Zizak, I.; Burghammer, M.; Metwalli, E.; Müller-Buschbaum, P.; Trebbin, M.; Förster, S.; Paris, O.; Roth, S. V.; Fratzl, P. A Customizable Software for Fast Reduction and Analysis of Large X-Ray Scattering Data Sets: Applications of the New DPDAK Package to Small-Angle X-Ray Scattering and Grazing-Incidence Small-Angle X-Ray Scattering. *J Appl Cryst* **2014**, *47* (5), 1797–1803. https://doi.org/10.1107/S1600576714019773.

(63) Shannon, R. D.; Prewitt, C. T. Effective Ionic Radii in Oxides and Fluorides. *Acta Crystallographica Section B* **1969**, *25* (5), 925–946. https://doi.org/10.1107/S0567740869003220.

(64) Fischer, A.; Schmitz, M.; Aichmayer, B.; Fratzl, P.; Faivre, D. Structural Purity of Magnetite Nanoparticles in Magnetotactic Bacteria. *J. R. Soc. Interface* **2011**, *8* (60), 1011–1018. https://doi.org/10.1098/rsif.2010.0576.

Figures

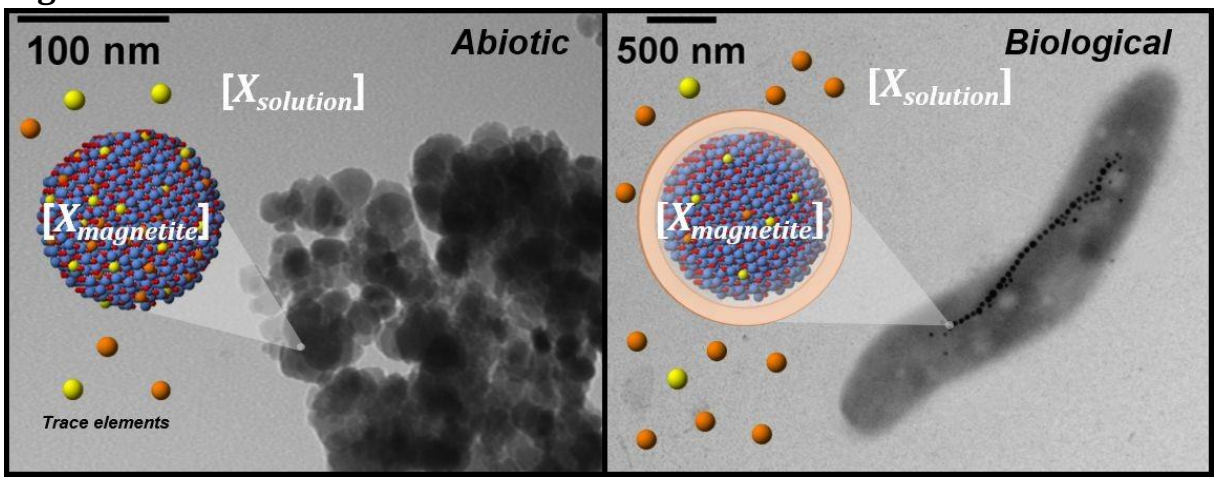

Scheme 1. Illustration of trace and minor elements analyzed in abiotic and biological magnetite. $[X_{magnetite}]$ refers to element concentration in magnetite, and $[X_{solution}]$ indicates the element concentration in the residual solution and residual growth medium in the case of abiotic and biological magnetite formation, respectively.

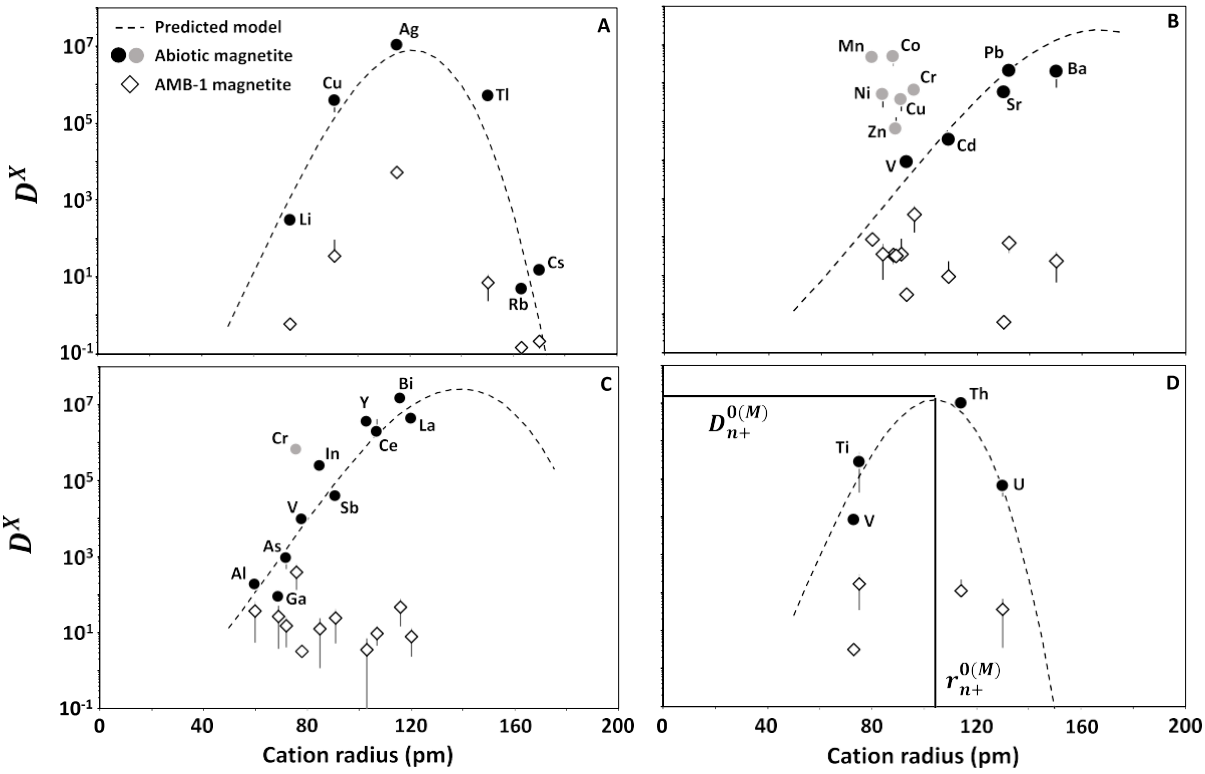

Figure 1. Partition coefficients (D^X) of (A) monovalent, (B) divalent, (C) trivalent and (D) tetravalent cations in the case of abiotic (black and grey circles) and biological (AMB-1, open diamonds) magnetite. Dashed line indicate the predicted values of D^X based on a lattice strain model (Eq. 2). Grey symbols point to 3d metals [Co(II), Cr(II), Cr(III), Cu(II), Mn(II), Ni(II), Zn(II)] showing variations from the predicted values in the abiotic precipitation of magnetite. Cation radius taken from Shannon and Prewitt and summarized in Table S10[63]. Black lines in (D) indicate the position of ideal cation radius ($r_{n+}^{0(M)}$) and strain-compensated partition coefficient ($D_{n+}^{0(M)}$).

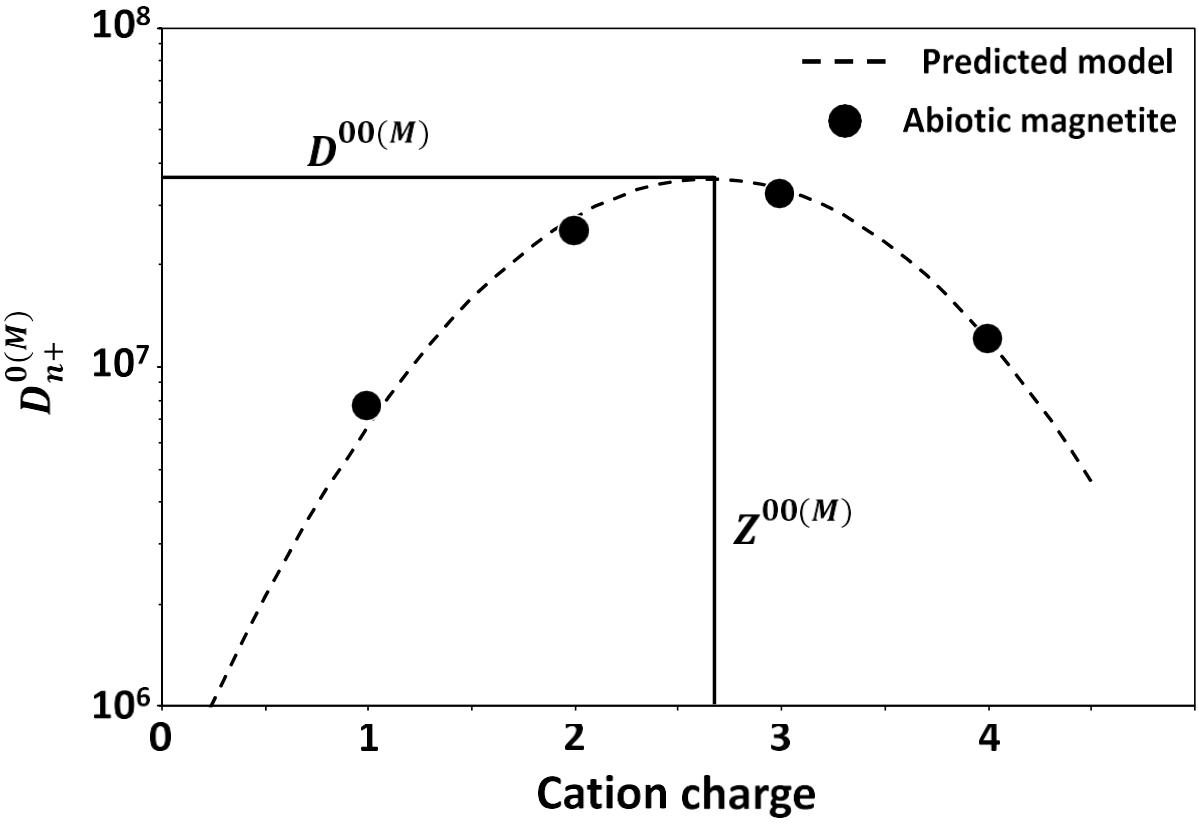

Figure 2. Strain-compensated partition coefficients ($D_{n+}^{0(M)}$) for each element valence extracted from Figs. 3A to 3D. The predicted model was calculated using Eq. 3 and considering published values of magnetite's dielectric constant of 55 and a lattice region with a radius of 9 nm (see Materials and Methods). Black lines indicate the position of ideal charge ($Z^{00(M)}$) and strain-compensated partition coefficient causing no electrostatic charging ($D^{00(M)}$).

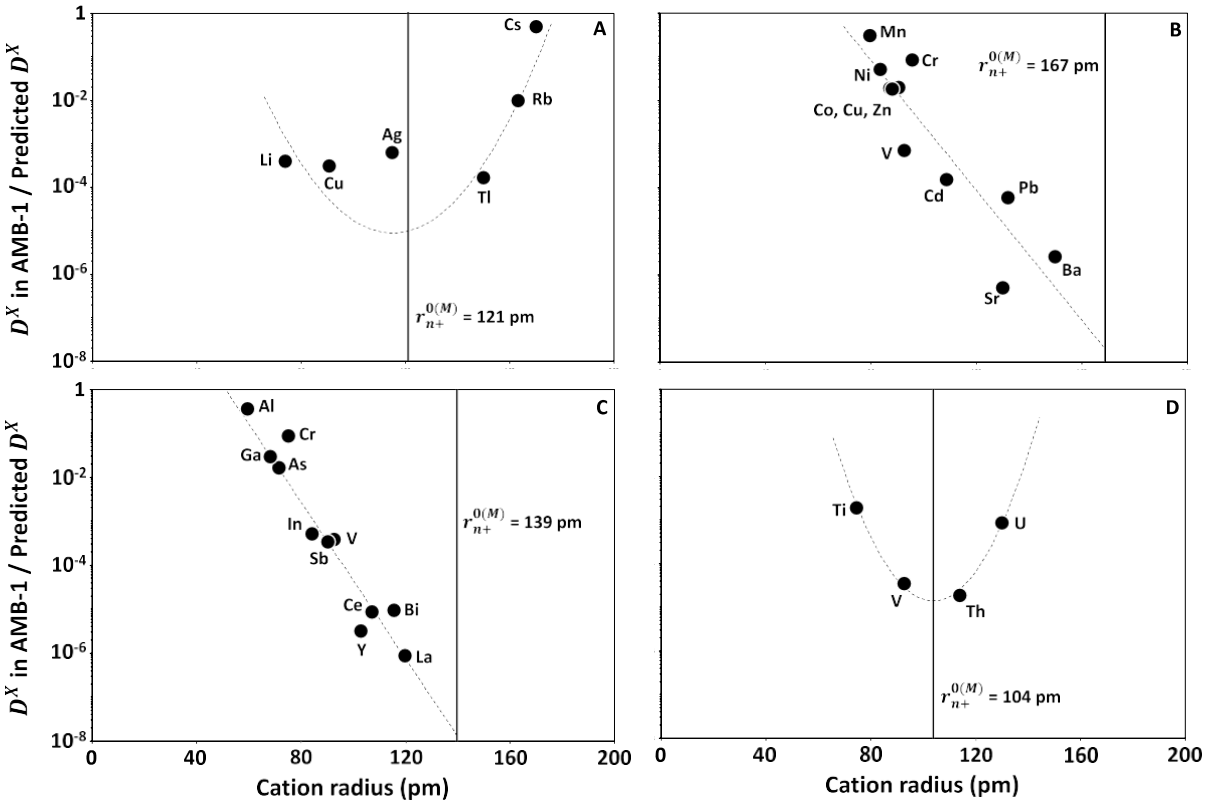

Figure 3. Biological D^X obtained from AMB-1 cultures normalized to the D^X predicted from lattice strain theory (Eq. 2) in the case of (A) monovalent, (B) divalent, (C) trivalent and (D) tetravalent elements. $r_{n+}^{0(M)}$ values reported here are extracted from Fig. 3 and Table S5.

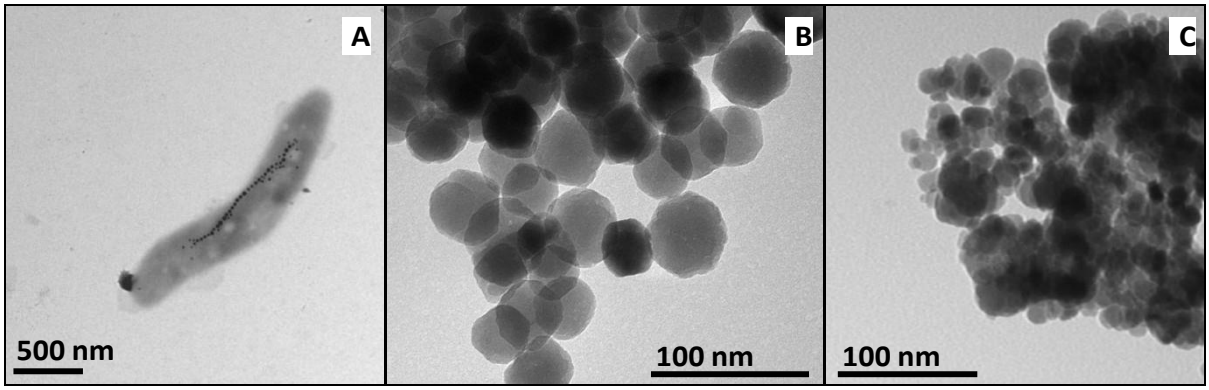

Figure 4. Transmission electron microscopy images of (A) MSR-1 bacteria containing magnetite nanoparticles, (B) biological magnetite nanoparticles extracted from MSR-1 and purified (see Materials and Methods), and (C) abiotic magnetite nanoparticles.

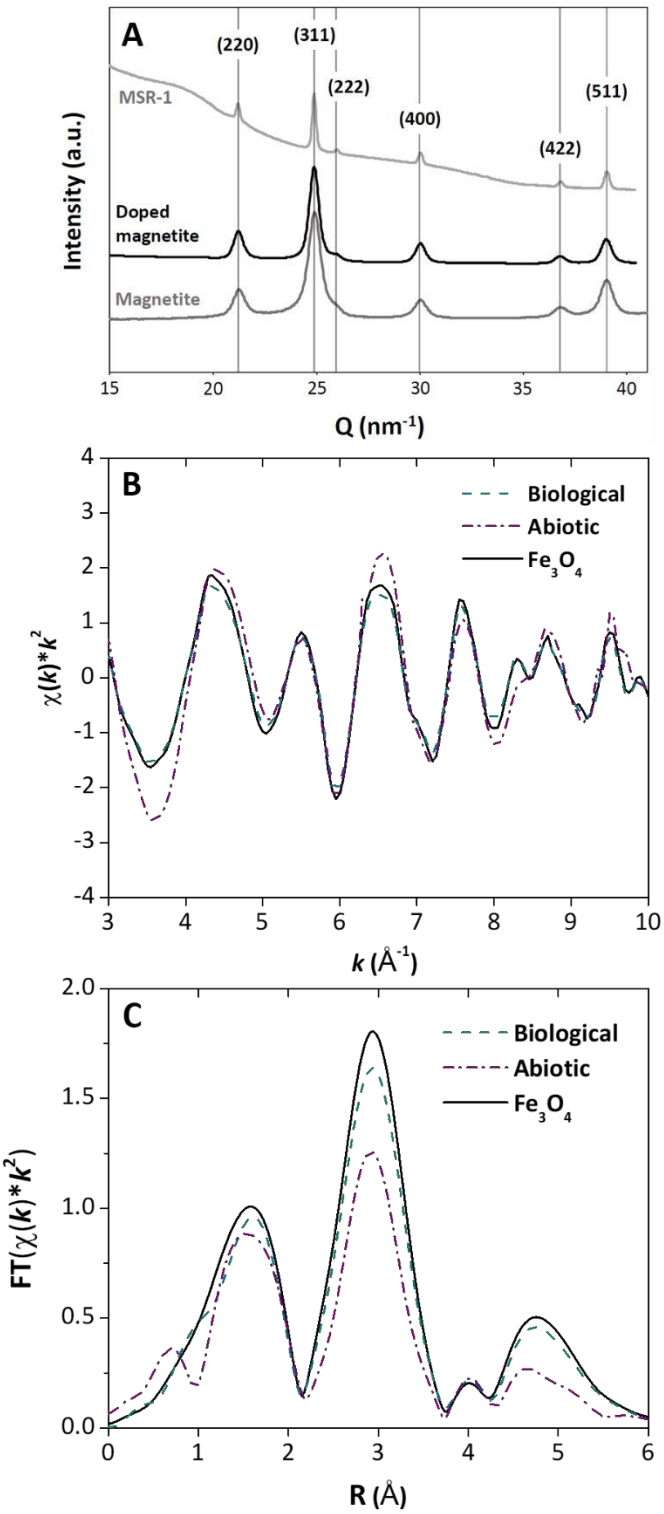

Figure 5. (A) X-ray diffractograms of doped abiotic and biological magnetite. An additional undoped abiotic magnetite reference is given for comparison. Abiotic magnetite shows all peaks typical of magnetite[64]. The broader peaks for abiotic magnetite can be explained by smaller

particles (see supplementary text). Fe K-edge XAS presented in the form of (B) *k*-space and (C) R-space spectra for magnetite reference, biological magnetite and abiotic magnetite.

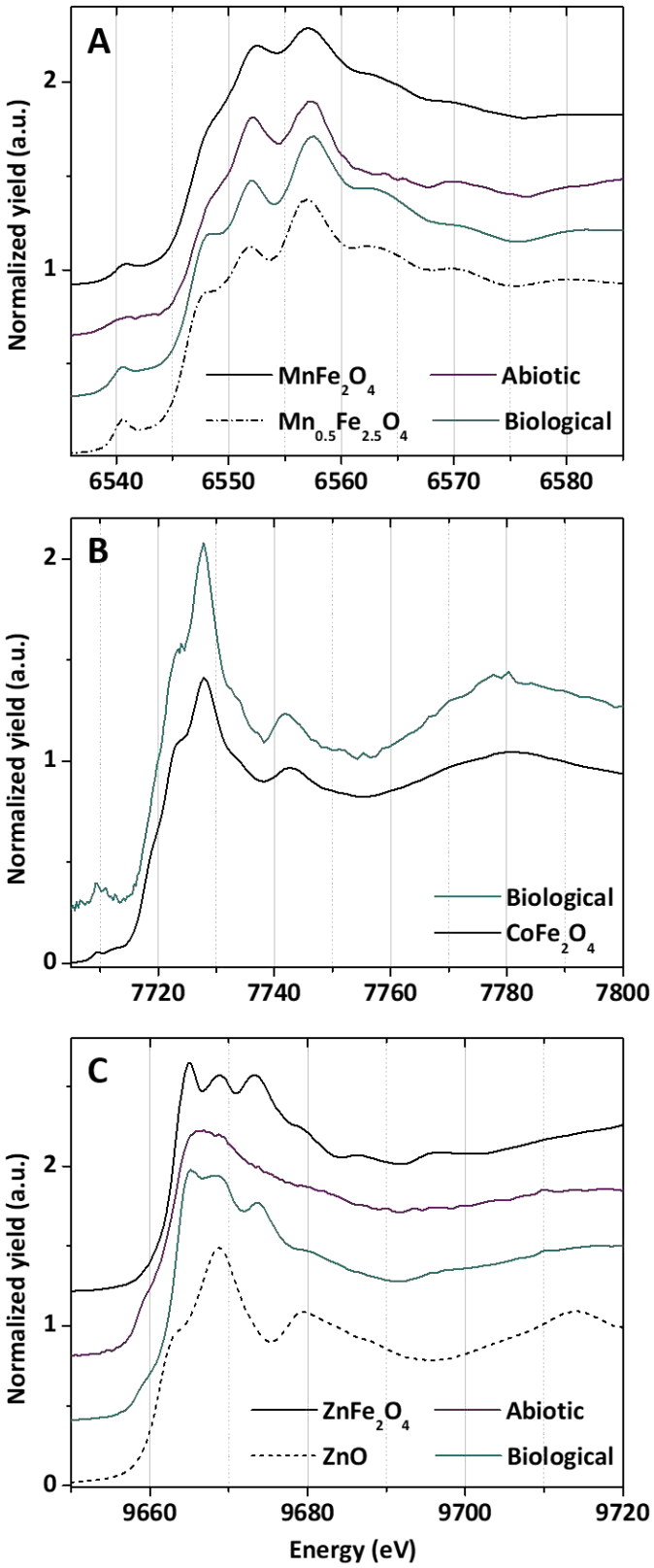
A
Normalized yield (a.u.)
2
1
6540
6550
6560
6570
6580
MnFe2O4
Mn0.5Fe2.5O4
Abiotic
Biological
B
Normalized yield (a.u.)
2
1
0
7720
7740
7760
7780
7800
Biological
CoFe2O4
C
Normalized yield (a.u.)
2
1
0
9660
9680
9700
9720
Energy (eV)
ZnFe2O4
ZnO
Abiotic
Biological

904

905

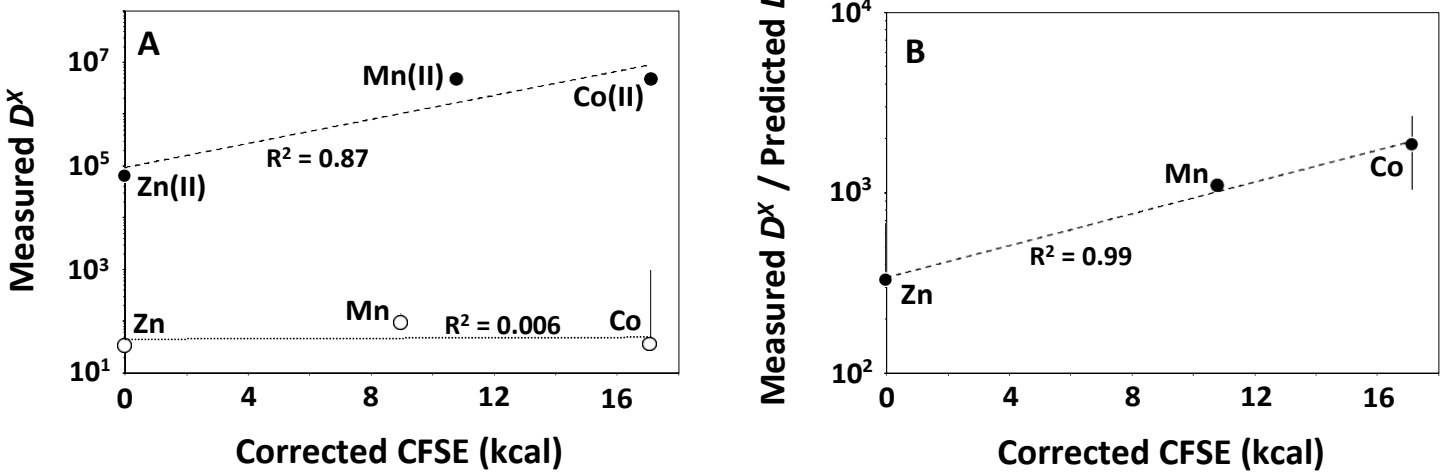

Figure 6. X-ray absorption near edge structure (XANES) of doped abiotic and biological magnetite nanoparticles with reference materials at (A) Mn K-edge (inset, pre-edge region), (B) Co K-edge and (C) Zn K-edge.

Figure 7. (A) Partition coefficients (D^X) and (B) ratio of measured partition coefficients and partition coefficients predicted from a lattice strain theory (Eq. 2) of Mn, Co and Zn represented against their XAS-corrected Crystal Field Stabilization Energy (CFSE). Black and open symbols represent abiotic and biological conditions, respectively.

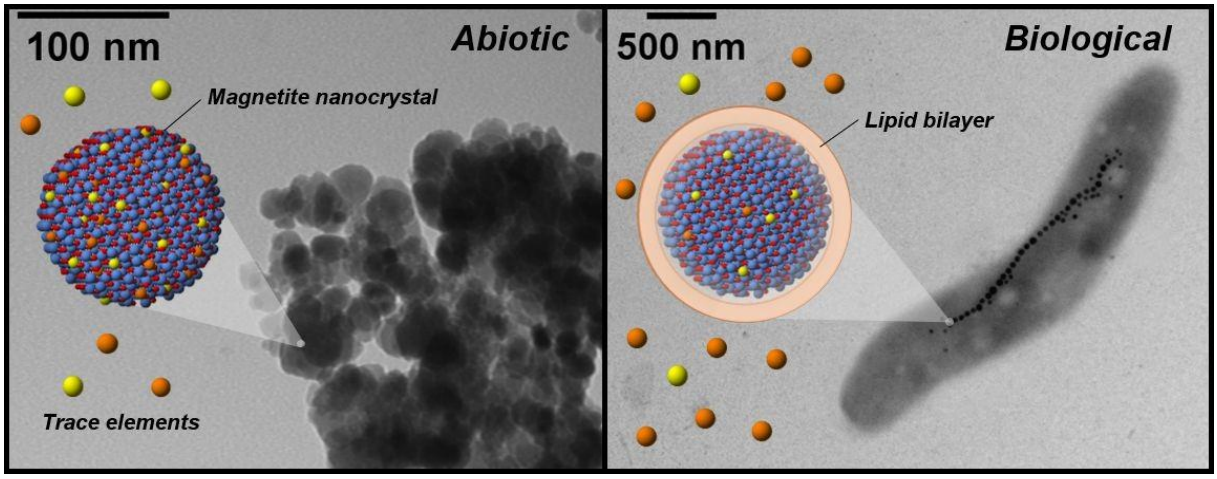
100 nm
Abiotic
Magnetite nanocrystal
Trace elements
500 nm
Biological
Lipid bilayer

ToC Image.